On-chip tunable quantum interference in a lithium niobate-on-insulator photonic integrated circuit

Journal Article

Author(s):
Maeder, Andreas; Finco, Giovanni; Kaufmann, Fabian; Sabatti, Alessandra; Kellner, Jost; Chapman, Robert J.; Grange, Rachel

Publication date:
2024-07

Permanent link:
https://doi.org/https://doi.org/10.3929/ethz-b-000673414

Originally published in:
Quantum Science and Technology 9(3), https://doi.org/10.1088/2058-9565/ad4b98

Funding acknowledgement:
- Lithium niobate-on-insulator photonics for linear optical quantum computing ()
- Maturing and scaling up fabrication of lithium-niobate-based integrated photonic sensors - LINIOS ()
- Integrated Phase Logic Networks ()
- Second-Order Nano-Oxides for Enhanced Nonlinear Photonics ()
- Novel Photonics Integrated Circuit (PIC) Technology building blocks ()

IOP Publishing   Quantum Sci. Technol. 9 (2024) 035040   https://doi.org/10.1088/2058-9565/ad4b98

Quantum Science and Technology

RECEIVED
16 November 2023

REVISED
26 April 2024

ACCEPTED FOR PUBLICATION
14 May 2024

PUBLISHED
28 May 2024

PAPER

On-chip tunable quantum interference in a lithium niobate-on-insulator photonic integrated circuit

Andreas Maeder*, Giovanni Finco, Fabian Kaufmann, Alessandra Sabatti, Jost Kellner, Robert J Chapman and Rachel Grange

Optical Nanomaterial Group, Institute for Quantum Electronics, Department of Physics, ETH Zurich, Zurich 8093, Switzerland

* Author to whom any correspondence should be addressed.

E-mail: maederan@phys.ethz.ch

Keywords: lithium niobate-on-insulator, Mach–Zehnder interferometer, Hong-Ou-Mandel interference, tunability, single photons, thermo-optic effect, integrated photonics

Abstract

Programmable interferometric circuits are at the heart of integrated quantum photonic processors. While the lithium niobate-on-insulator platform has the potential to advance integrated quantum photonics due to its strong nonlinearity and tight mode confinement, the demonstration of reconfigurable two-photon interference has not yet been achieved. Here, we design, fabricate and characterize the building block of such interferometric networks in the form of a 2×2 Mach–Zehnder Interferometer. We use a thermo-optic phase shifter to achieve stable performance with a power consumption of $P_\pi = 44.4$ mW and sub-microsecond switching times. We demonstrate the effectiveness of our device for quantum applications by measuring single-photon routing with up to 34 dB extinction ratio. We show Hong-Ou-Mandel interference with fully tunable visibilities reaching a maximum value of $97.4 \pm 1.0\%$. As part of large scale quantum photonic circuits, this building block will facilitate reconfigurable and tunable photonic processing units integrated alongside non-classical light sources.

1. Introduction

Photonic quantum computing promises to surpass classical computing by exploiting superposition and entanglement. Photons have unique advantages for quantum computing, such as their very long coherence lengths and the ability to be transmitted in optical fibers with low loss, which makes them ideal carriers of quantum information. Important applications in photonic quantum computing include boson sampling and linear optical quantum computing [1, 2]. Fundamentally, all photonic quantum information processing applications require quantum light sources, quantum photonic processors based on interferometric circuits and detection [3, 4].

Universal quantum photonic processing can be realized using networks of tunable beam splitters (TBS) [5]. Such quantum photonic processing units have been successfully demonstrated with tunable Mach–Zehnder interferometers (MZIs) as their central building block on silicon [6], silica-on-silicon [7], and silicon nitride [8] integrated photonics platforms. Additionally, for realization of standalone quantum photonics circuits, the integration of efficient quantum light sources is equally important. While silicon and silicon nitride based platforms can use spontaneous four wave mixing sources [6], they require either high pump powers or long waveguides for efficient operation. Also pump filtering is challenging since the pump wavelength is typically close to the wavelength of the generated photons. Sources based on spontaneous parametric downconversion (SPDC) are beneficial in this regard, however this negates the use of photonics platforms based on centrosymmetric materials such as silicon and silicon nitride.

In this context, lithium niobate-on-insulator (LNOI) is emerging as a promising platform in the pursuit of efficient quantum information processing on a chip-scale. LNOI features a large second order nonlinearity, a high electro-optic (EO) coefficient, a large transparency window from 0.4 to 4.5 µm, and does not suffer from two photon absorption [9]. Because of advances in nanofabrication techniques, waveguide circuits with propagation losses as low as 1 dB m^{-1} at both visible and near-infrared wavelengths have been realized [10–12]. Although the fabrication has yet to reach the same maturity as more established platforms, these advances paved the way for high-performance photonic devices based on LNOI, including EO modulators [13, 14], switches [15] and frequency combs [16]. Furthermore, the fabrication of periodically poled waveguides also allows for integration of efficient and high brightness quantum light sources directly on-chip [17]. This capability not only enables monolithic quantum circuits, but also eliminates losses at interfaces between source and processor chips, making it a key enabler for on-chip quantum information processing.

Reconfigurable quantum photonic processing units can be on LNOI using MZIs with EO phase shifters [18]. However, stability is an important criterion for any tuning mechanism. DC drift effects in EO devices on LNOI are a serious problem in this regard [19, 20]. Thus, thermo-optic phase shifters (TOPSs), which are widely used in other integrated photonics platforms, have gained interest in LNOI and have shown excellent performance, especially in terms of stability [21, 22]. Furthermore, TOPS typically have a smaller footprint than EO phase shifters [18], which is advantageous for the implementation of large scale circuits.

In this work, we present a thermo-optically tunable MZI as a versatile building block on the LNOI platform, and demonstrate its applicability for quantum information experiments by interfering single photons from an external SPDC source. We start by discussing the device parameters studied with simulations before characterizing the device fabricated in-house in both a classical and a quantum regime. In our experiments we are able to measure high extinction ratios above 31 dB in both the cross- and bar-port response with a continuous wave (CW) telecom laser. Furthermore we show record low switching times of 0.7 µs with TOPS on the LNOI platform. Finally, we present two key applications for quantum optic experiments. First, we demonstrate routing of single photons with a bandwidth of 12 nm reaching up to 34 dB suppression of the countrate. Furthermore, we show on-chip Hong-Ou-Mandel (HOM) interference, where we are able to continuously tune the visibility by changing the applied voltage. In particular we are able to reduce it until no interference dip is observable, and maximize it to a value of $97.4 \pm 1.0\%$, demonstrating the full tunability of our device. Our results create a strong foundation for integration of this building block alongside single photon sources into large scale LNOI circuits for quantum applications, such as scattershot or Gaussian boson sampling [23, 24].

2. Design and simulation

The basic schematic of the 2×2 MZI structure studied in this work is shown in figure 1(a). The main building blocks are two directional couplers to split and recombine the light, and a TOPS for active control of the phase difference between the two interferometer arms. A schematic of the cross-section through a directional coupler is shown in figure 1(b), where two identical waveguides of width w_{wg} separated by a gap g_c are used. A SiO_2 cladding of thickness h_{TOX} is used to both protect the optical circuitry and leverage the less confined modes which decrease the required coupling length L_c. On both arms of the interferometer a gold strip is placed above the waveguide as shown in the cross-section in figure 1(c). This strip has width w_h, height h_h, and length $L_h = L_s$, identical to the arm length of the interferometer, and acts as a TOPS upon application of a voltage U. For in- and out-coupling of light, focused grating couplers monolithically integrated in LNOI are used.

An optical microscope image of the final device is shown in figure 1(d). Note that the fabricated device features TOPS on both arms, however all the results reported here only ever use one. Additionally, scanning electron microscope (SEM) images of the coupling region prior to cladding deposition, and a gold heater are shown in figures 1(e) and (f) respectively.

One of the key metrics of 2×2 MZIs is the extinction ratio ER_p, that is the ratio of the transmitted power between the on-state and the off-state of a port p. We can theoretically model the response of this system using a transfer matrix method. From this the extinction ratio of both cross- and bar-port can be extracted as (see appendix A for a more detailed calculation):

$$\mathrm{ER}_{\mathrm{cross}} = \left(\frac{1+a}{1-a}\right)^2, \qquad \mathrm{ER}_{\mathrm{bar}} = \left(\frac{R+a(1-R)}{R-a(1-R)}\right)^2. \tag{1}$$

Here, the reflectivity R is the fraction of power reflected by each directional coupler, which are assumed to be identical and loss-less, and a is a loss factor accounting for possible imbalance between the two interferometer arms. These equations show, that $\mathrm{ER}_{\mathrm{cross}}$ is independent of R and approaches infinity in the case of no loss imbalance ($a = 1$). However, for $\mathrm{ER}_{\mathrm{bar}}$, we find that it is maximized if $R = 0.5$. Hence, it is of crucial importance for the device performance to have 50 : 50 splitting at both couplers.

To model the directional couplers, we use a coupled mode theory (CMT) approach [25], and compute mode overlap integrals of a specified cross-sectional geometry. In our design, a coupler consists of two

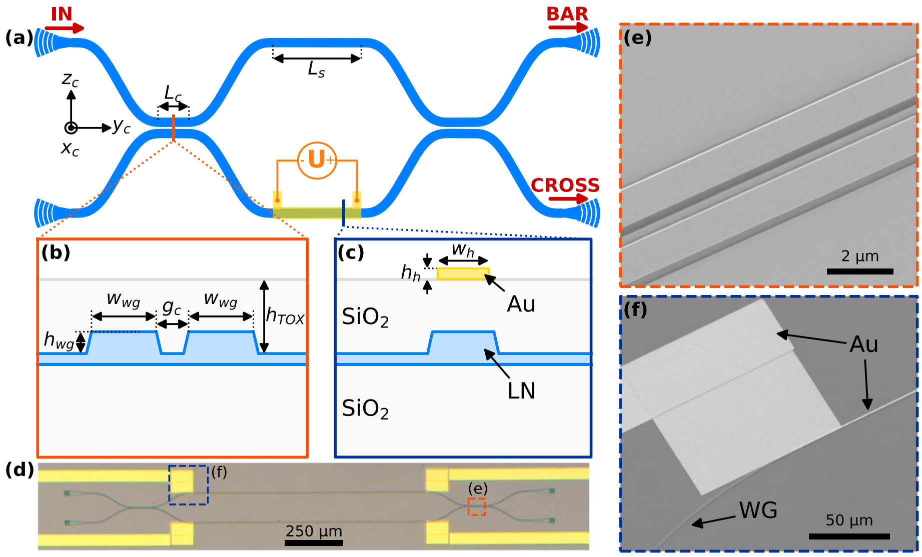

Figure 1. (a) Schematic overview of the investigated 2×2 MZI. The coordinate system indicates the orientation of the LNOI crystal. Cross-sections of (b) the coupling regions and (c) the phase shift region with a TOPS are included. (d) Optical microscope image of the MZI. The dashed lines indicate the regions where detailed SEM images of (e) a coupling region with two co-propagating LN waveguides prior to cladding deposition, and (f) a gold (Au) strip heater including pads and routing layer after cladding deposition. The outline of the buried waveguide (WG) is also visible in (f).

waveguides approaching each other with sinebends, followed by a straight co-propagating section featuring a fixed gap g_c, after which the waveguides split again with the same sinebend as for the approach. We use constant sinebend parameters $L_{sb} = 200\,\mu$m and $D_{sb} = 62.6\,\mu\mu$m as well as $g_c = 600$ nm throughout all investigated circuits. This entire coupling region is parametrized by a function $g(y)$ which gives the gap between the waveguides as a function of the position y in propagation direction (see figure 2(a)). We evaluate this function at discrete points y_i and determine the corresponding coupling coefficients for each cross-sectional gap $g(y_i)$. Subsequently, we use these coupling coefficients to numerically solve the coupled mode equations (see appendix B) with coefficients varying along the propagation direction. A typical result obtained with these simulations is shown in figure 2(b) for the fundamental quasi-TE mode at a wavelength of $\lambda = 1550$ nm, and a straight coupling length of $L_c = 46\,\mu$m. We can see, that a significant amount of coupling happens outside of the straight section of the coupler. Besides taking coupling in the bends into account, we also find that accounting for the trenching generated in our fabrication process is important for accurate device modeling (see appendix B for more details). Therefore, all the simulations presented here use an effective etch depth of $h_{wg} = 235$ nm of a 300 nm thick LN film.

We repeat simulations at $\lambda = 1550$ nm for a discrete set of coupling lengths. The output power after propagation through the full directional coupler is shown in figure 2(c) for both waveguides (circle markers, with dotted lines). A length $L_{0.5} = 37.6\,\mu$m for 50 : 50 splitting is extracted from these simulations. We can compare this to the length we would obtain when neglecting coupling in the bends. This is equivalent to a simulation with a constant gap function $g(y) = g_c$ also shown in figure 2(c) (solid lines). This approach yields a substantially different result of $L_{0.5} = 61.3\,\mu$m. This difference of around $24\,\mu$m underlines the necessity of accounting for light coupling in the approaching parts of the directional couplers. Furthermore, these results show that *a priori* modeling of interferometric structures is important to achieve good device performance. This is particularly relevant considering that for large scale circuits, making replica of the same design with slightly varying device parameters is not a feasible approach. Accurate prediction of device behavior can therefore decrease the number of iterations when optimizing a device design.

The second important building block, the TOPS, is simulated using the finite element method, where 3D heat transfer simulations are coupled to a 2D mode solver to solve for the fundamental quasi-TE mode of a single waveguide. A typical temperature distribution is shown in figure 2(d) and we experimentally measure it as well as discuss implications in terms of crosstalk in appendix C. From this simulation we can extract the expected power required for a π phase shift P_π (see also our previous work [21] for more details). The most important cross-section parameter to investigate is the cladding thickness h_{TOX}, since a lower thickness means both higher efficiency but also higher insertion loss due to light absorption in the metallic heater. In figure 2(e) we show the dependence of the TOPS insertion loss and P_π on h_{TOX} for a heater of with

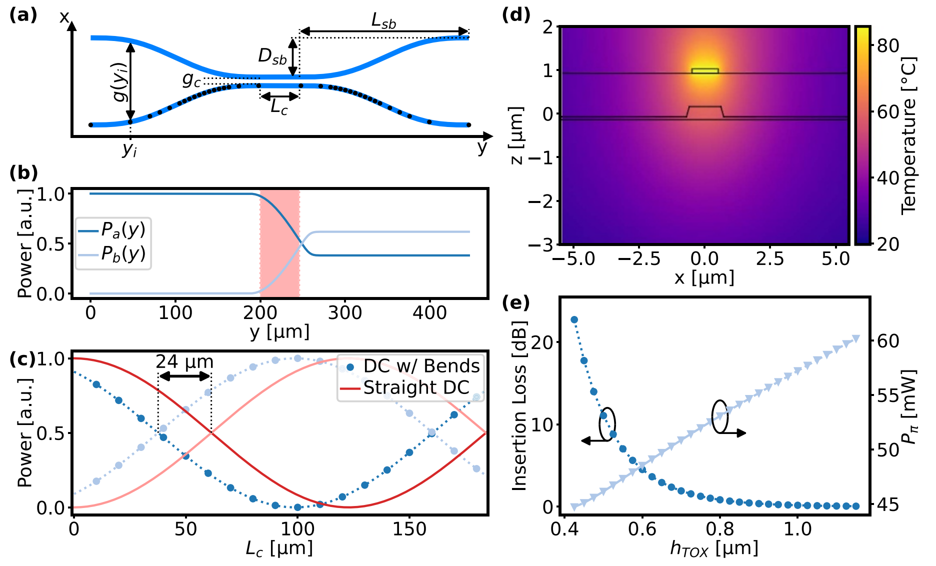

Figure 2. (a) Schematic view of the directional coupler design with the relevant parameters. (b) Power evolution in two co-propagating waveguides obtained with the CMT approach. The highlighted region corresponds to the $L_c = 46\,\mu$m long section where $g(y) = g_c = 600$ nm. (c) Simulation of the power evolution in a directional coupler (including the bends) as a function of L_c (points with dashed lines) and in a directional coupler with constant gap g_c. The darker and lighter colors show the powers $P_a(y)$ and $P_b(y)$ respectively. (d) Simulated temperature cross-section through a TOPS. (e) Phase shift power P_π and insertion loss of a TOPS with $L_h = 1$ mm as a function of the oxide cladding height h_{TOX}.

dimensions $L_h = 1$ mm, $w_h = 1\,\mu$m and $h_h = 100$ nm. For $h_{\mathrm{TOX}} = 1\,\mu$m the insertion loss is 0.16 dB and $P_\pi = 57.2$ mW, which compares well to current silicon foundry state of the art for TOPS without undercuts [26], considering that the thermo-optic coefficient of LN is roughly a factor of 3 lower than the one of silicon [26, 27].

3. Fabrication and classical characterization

Based on simulation and design presented above, we fabricated a 2×2 MZI on a 300 nm *x*-cut LNOI chip. The waveguides were patterned using electron-beam lithography and argon ion milling in an inductively coupled plasma etching tool [28]. All waveguides have a width $w_{\mathrm{wg}} = 1200$ nm and are etched 200 nm, leading to an estimated effective waveguide height $h_{\mathrm{wg}} = 235$ nm (see also appendix B). The directional couplers use the design parameters $g_c = 600$ nm and $L_c = 46\,\mu$m. Due to experimental constraints, the ideal device for $\lambda = 1550$ nm was not accessible. Subsequently, a SiO_2 layer was deposited using plasma enhanced chemical vapor deposition after which the gold heater was added using another electron beam lithography step followed by electron beam evaporation of a 100 nm thick gold layer and a standard lift-off process. Then, a second metal layer to route the contacts to the chip edge was deposited the same way (see also figure 1(f)). Finally, these contacts were wirebonded to a printed circuit board (PCB) for electrical connection to the device.

Classical characterization was performed using the setup shown in figure 3(a). A tunable telecom laser source is coupled to the device using monolithically integrated grating couplers and standard SMF28 fibers in custom fiber holders. A polarization controller is used on the input to optimize the polarization for maximum coupling to the fundamental TE mode. For detection either a high dynamic range powermeter (PM) or a photodetector (PD) connected to an oscilloscope (OSC) is used. For improved signal-to-noise ratio of the signal we use an electrical low-pass filter (LPF). A 16-bit electronic driver with the capability to supply up to 50 mA to the TOPS is connected to the PCB.

First, we characterized the thermo-optic response of the system using the PM. In figure 3(b) the cross- and bar-port response at $\lambda = 1516$ nm is shown. Both ports exhibit extinction ratios above 31 dB which indicates that the two couplers are close to perfect 50 : 50 splitting at this wavelength. This matches with the wavelength dependent simulations shown in appendix B. From this measurement, a phase shift power of $P_\pi = 44.4$ mW is extracted. This power corresponds to a CMOS-compatible voltage below 5 V. there is no quantitative agreement between measurement and simulation, the experimentally obtained P_π falls within the range that simulations have predicted. The simulation model would need to be revised to include effects such as thermal contact resistances at material interfaces and reduced thermal conductivities in thin film

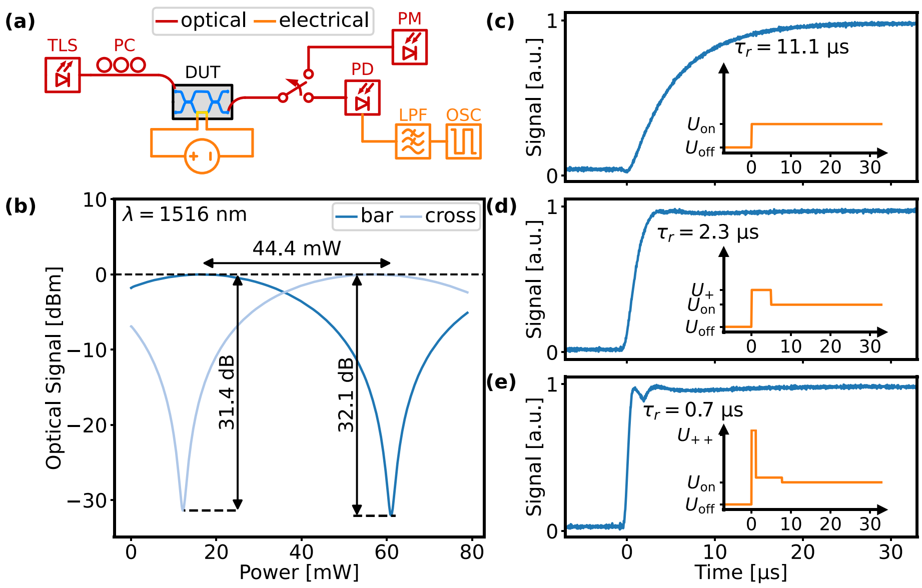

Figure 3. (a) Experimental setup for classical characterization. See main text for a detailed description. (b) MZI characterization showing transfer function of bar- and cross-port with high extinction ratios above 31 dB for both ports at $P_\pi = 44.4$ mW. (c) Step response to applied square signal between $U_{\mathrm{off}} = 4.4$ V and $U_{\mathrm{on}} = 6.5$ V with a rise time of $\tau_r = 11.1$ µs. Reduced rise times are shown for (d) single overdrive voltage peak ($\tau_r = 2.3$ µs) and (e) more advanced overdrive voltage signal leading to $\tau_r = 0.7$ µs.

materials, to obtain also quantitative agreement. However, these material properties are not readily available, and would have to be individually measured which is beyond the scope of this work.

The dynamic response of the device is investigated by measuring its response to a square signal ($f = 1$ kHz) applied between $U_{\mathrm{off}} = 4.4$ V and $U_{\mathrm{on}} = 6.5$ V with the PD. Figure 3(c) shows the optical response to the applied step which has a rise time of $\tau_r = 11.1$ µs. This is already as good as or better than comparable silicon foundry TOPS [26]. We employed a common approach to reduce this number further, which is to apply an initial overdrive voltage U_+ for a duration δt_1 [29, 30]. With this approach, the rise time is reduced by a factor of 5 to $\tau_r = 2.3$ µs with $U_+ = 7.9$ V applied for $\delta t_1 = 5$ µs as shown in figure 3(d). By applying an initial voltage peak of height $U_{++} = 11$ V for a shorter time of $\delta t_1 = 1.1$ µs, which is then reduced to $U_{\mathrm{on}} + 0.1(U_{++} - U_{\mathrm{on}})$ and held for $\delta t_2 = 7.7$ µs, the rise time was further decreased to 0.7 µs as shown in figure 3(e). With this method we show, that sub-microsecond rise times are possible for thermo-optic switching on the LNOI platform. Although there is a slight peak that appears after the initial rising edge in figure 3(e), this approach could be refined further by applying more complex electrical waveforms to mitigate this.

4. Single photon experiments

The LNOI 2×2 MZI presented here is a fundamental building block for quantum photonic processors based on interferometric circuits. While its classical characteristics have been presented above, it is important to verify the performance with non-classical light sources, such as SPDC photon pair sources, since their spectral bandwidth is typically much broader than a CW laser.

Here, we use an SPDC photon pair source based on a β-barium borate (BBO)-crystal continuously pumped at $\lambda_{\mathrm{p}} = 775$ nm in a free-space setup. The photon pairs were spectrally filtered with a 12 nm bandpass filter, separated by polarization and subsequently fiber-coupled which allows us to couple them to the MZI in the same setup as for the classical characterization. More details on the photon pair source are given in appendix D. To detect the single photons, we used fiber-coupled superconducting nanowire single photon detectors (SNSPDs).

In a first experiment illustrated in figure 4(a), we sent one photon directly to the detector while the other one was coupled to the MZI and then to the detector. With a time-to-digital converter (TDC), coincidence measurements between the two SNSPD channels are conducted. With this measurement, we can observe routing of single photons controlled by the voltage applied to the TOPS. The result for the photons collected from either the cross- or the bar-port are shown in figure 4(b). We also show the classical characterization result at $\lambda = 1550$ nm as solid lines in the same plot. The extinction ratios of 34.0 dB (cross-port) and 13.4 dB (bar-port) measured for the single photon experiment correspond well with the ones obtained with

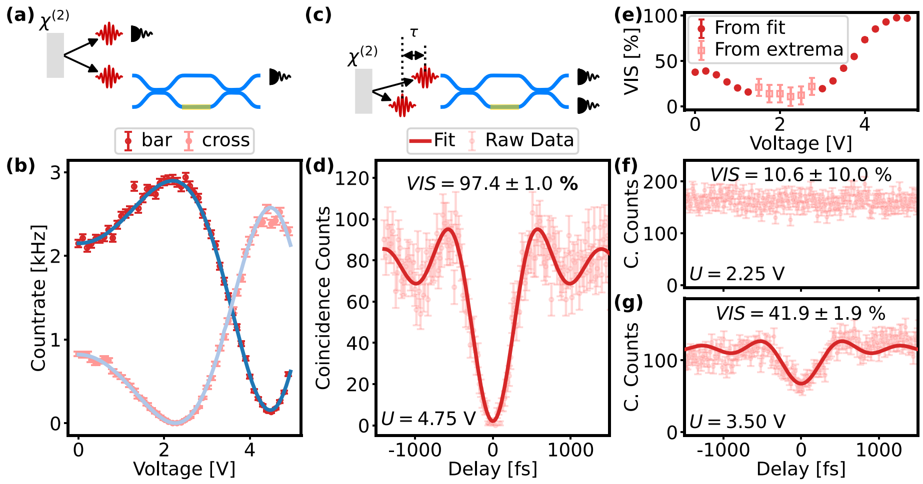

Figure 4. (a) Schematic of single photon routing experiment. (b) Result of single photon routing showing switching between cross- and bar-port with extinction up to 34 dB. The solid lines show the classical result measured with a CW laser at $\lambda = 1550$ nm. (c) Schematic of HOM interference experiment. HOM interference measurements are shown for applied voltages of (d) $U = 4.75$ V, (f) $U = 2.25$ V and (g) $U = 3.5$ V. The solid lines in (d), (f) and (g) are fits to the experimental data. (e) The visibility *VIS* of the HOM dip for different applied voltages. It is tuned between $10.6 \pm 10.0\%$ and $97.4 \pm 1.0\%$.

classical laser light which are 36.2 dB and 12.6 dB for the two ports respectively. They do not reach the symmetry shown in 3(b) since the splitters are not perfectly 50 : 50 at $\lambda = 1550$ nm, which is confirmed by the simulations shown in figure 2(b) and appendix B. This result shows that the device is able to route single photons between two ports, suppressing the photon counts by up to 34 dB. Moreover, it shows that the splitters do not limit the device performance even though the photons have a higher bandwidth.

Finally, a 2×2 MZI can be used to realize HOM interference, where it acts as a TBS, which is a key building block for linear optical quantum computing [2]. To perform this experiment, we switched from using single fibers to fiber arrays to couple the two input and two output ports simultaneously. We sent both photons from the source through a fiber-coupled tunable delay line and subsequently onto the splitter (see figure 4(c)). By tuning the delay τ, we are then able to observe on-chip HOM interference. When we apply different voltages to the TOPS, we tune the overall splitting ratio of the on-chip device, which leads to tuning of the visibilities [31].

We show results of the HOM interference dip for selected voltages in figures 4(d), (f) and (g). In figure 4(e), we show the obtained visibilities as a function of the applied voltage. They are obtained from a sinc-shaped fit to the experimental data, where possible. The fit is shown in figures 4(d) and (g) (solid line). For the measurement points between 1.5 V and 2.75 V, the fit does not perform reliably, as there is no observable interference dip (see figure 4(f)). To get a quantitative estimate of the visibility nonethelss, we used the maximum and minimum coincidence count rate to estimate an upper bound on the visibility. The maximum visibility of $97.4 \pm 1.0\%$ was observed for $U = 4.75$ V and the minimum estimated upper bound on the visibility is $10.6 \pm 10.0\%$ for a voltage of 2.25 V. A more detailed explanation on the fitting procedure along with all the HOM interference dips obtained is given in appendix E.

There is a discrepancy between the single photon routing measurements reported in figure 4(b) and the HOM measurements. According to the single photon routing measurements, the anticipated voltage at which the MZI acts as an overall 50 : 50 splitter should be around 3.5 V. However, this expectation does not match the result from the HOM experiments. We attribute this inconsistency to gradual temperature variations occurring on the chip or within the sample mount. In this experiment, the coincidence count rates are on the order of a few Hz, leading to an overall measurement duration (including the voltage sweep) of several hours. Although our sample holder is temperature controlled with a Peltier element, we do not monitor temperature on or close to the chip. We are confident that by enhancing our sample holder design and implementing more robust thermal control measures, we can mitigate these long-term stability issues.

The full tunability of the visibility of the HOM interference dip, in combination with the single photon routing experiment and supported by the classical characterization, shows that this building block is ideally suited for integration with on-chip SPDC sources. It also demonstrates, that the increased bandwidth of the photons compared to a classical CW laser source has only a small influence on the performance.

Table 1. Comparison table of selected tunable MZIs used for quantum applications on different platforms. We compare power required for π phase shift P_π, extinction ratio (ER), and the length of the active phase shift region (L_s). For the work using EO phase shifters, we give the voltage V_π required for a π phase shift instead of P_π.

Platform	Heater	P_π (mW)	ER (dB)	L_s (mm)	Source
SOI	Ti	12.5	35	0.1	[6]
Silica	Au	234	17[a]	20	[32]
Silica	n/a	347[b]	20[a]	9.7	[33]
SiN	Pt	385	n/a	1.0	[34]
LNOI (EO)	n/a	n/a ($V_\pi = 4.5V$)	21	1.3	[18]
LNOI (TO)	Au	44.4	34	1.0	This Work

[a] Computed from fringe visibility.

[b] Estimated from reported voltage-current data.

5. Conclusion and outlook

In conclusion, we have demonstrated a 2×2 MZI monolithically integrated on the LNOI platform. The device uses TOPS to introduce phase shifts which feature a low $P_\pi = 44.4$ mW achieved with CMOS compatible voltages below 5 V. The power consumption is among the lowest ever reported in comparable structures [35, 36], and can be boosted using thermal isolation trenches [37]. We showed that the thermo-optically tuned MZI can reach extinction ratios above 31 dB symmetrically on both ports and reached optical response times as low as 0.7 µs by employing an overdrive protocol. This is, to the best of our knowledge, the first demonstration of sub-microsecond response times using TOPS on the LNOI platform.

Apart from excellent classical performance, we also characterized the device with a non-classical light source. We showed its use in routing of single photons with 12 nm bandwidth, where we were able to suppress them by 34 dB, which is higher than devices have previously achieved on other platforms [38, 39]. For applications where ultra-high extinction ratios are desired, cascading MZI structures is an approach that has been demonstrated classically [40, 41]. However, this comes at the cost of an increased footprint and two additional phases which require electrical connections. Hence we believe that using passive splitters whenever possible is favorable for scalability.

Finally, we also investigated on-chip HOM interference and observed fully tunable visibilities as high as $97.4 \pm 1.0\%$. By tuning the voltage we are able to reduce the visibility to a point where there is no interference dip observable. This indicates that the MZI can be used as a TBS for integration into interferometric circuitry for quantum photonic processing. Since TOPS are employed for phase control, the footprint of such circuits can be significantly reduced as compared to electro-optically tuned devices [18]. If however the ultra-high speed switching properties of the EO effect is a strict requirement for an application, the waveguide circuit presented in this work can still be used and similar extinction ratios and performance metrics are expected. Further investigations into fully etched devices could lead to even further footprint reduction as better mode confinement would support tighter bending of the waveguides [42].

In table 1 we compare this work to a selection of quantum experiments reported in literature, that either demonstrate or leverage tunable quantum interference in an on-chip MZI. Our device performs similarly or better in terms of power consumption, extinction ratio and size (measured by the length of the phase shift region L_S).

Despite the fact that the LNOI platform has yet to prove its potential for scalable fabrication, the prospect of integrating bright non-classical light sources with small footprint processing units and integrated single photon detectors [43, 44] shows the potential of the LNOI platform. These capabilities enable monolithic integration of quantum photonic experiments onto a single chip, which represents a significant step towards the realization of quantum technology's promising future.

Data availability statement

The data that support the findings of this study are available upon reasonable request from the authors.

Acknowledgments

We acknowledge support for fabrication and characterization of our samples from the Scientific Center of Optical and Electron Microscopy ScopeM and from the cleanroom facilities BRNC and FIRST of ETH Zurich and IBM Ruschlikon. This work was partially funded by the Swiss National Science Foundation under the Ambizione Fellowship Program (Project Number 208707), the European Space Agency (Project Numbers 4000137426 and 4000136423), the Swiss National Science Foundation under the Bridge Program (Project

Number 194693), the Swiss National Science Foundation Sinergia (Integrated Phase Logic Networks, Project Number CRSII5_206008), Innosuisse (PHORESTA, Project Number 106.733 IP-ENG), the European Research Council (Project Number 714837), and Horizon 2020 (ELENA Consortium, Project Number 101016138).

Conflict of interest

The authors declare no competing financial or non-financial interests.

Appendix A. 2 × 2 MZI response function

A 2 × 2 MZI consists of two directional couplers and an actively (by TO or EO effect) or passively (by adding imbalance) induced phase shift $\Delta\varphi$. Depending on the magintude of this phase shift, the MZI will be in a different output state.

Based on these three components we can model the switch in a transfer matrix approach as the matrix product of three individual matrices and obtain the output fields in the two waveguides $\mathbf{E}_{\mathrm{out}}$ dependent on the input fields $\mathbf{E}_{\mathrm{in}}$ as

$$\mathbf{E}_{\mathrm{out}} = \begin{pmatrix} \sqrt{R_2} & i\sqrt{T_2} \\ i\sqrt{T_2} & \sqrt{R_2} \end{pmatrix} \begin{pmatrix} 1 & 0 \\ 0 & a e^{\mathrm{i}\Delta\varphi} \end{pmatrix} \begin{pmatrix} \sqrt{R_1} & i\sqrt{T_1} \\ i\sqrt{T_1} & \sqrt{R_1} \end{pmatrix} \mathbf{E}_{\mathrm{in}}, \tag{A.1}$$

where R_i is the reflectivity and T_i the transmissivity of splitter i ($i = 1,2$), and a is a loss factor accounting for loss imbalance between the two arms. Assuming light is only input on the first port, i.e. $\mathbf{E}_{\mathrm{in}} = \begin{pmatrix} 1 \\ 0 \end{pmatrix}$, we get the following output powers in the two output ports:

$$P_{\mathrm{bar}} = |\mathbf{E}_{\mathrm{out},1}|^2 = R_1R_2 + a^2T_1T_2 - 2a\sqrt{R_1R_2T_1T_2}\cos(\Delta\varphi) \tag{A.2}$$

$$P_{\mathrm{cross}} = |\mathbf{E}_{\mathrm{out},2}|^2 = R_2T_1 + a^2R_1T_2 + 2a\sqrt{R_1R_2T_1T_2}\cos(\Delta\varphi). \tag{A.3}$$

Assuming lossless ($T_i = 1 - R_i$) and symmetric ($R_1 = R_2 \equiv R$) couplers will simplify these expressions to

$$P_{\mathrm{bar}} = R^2 + a^2(1-R)^2 - 2aR(1-R)\cos(\Delta\varphi), \tag{A.4}$$

$$P_{\mathrm{cross}} = (1-R)R + a^2(1-R)R + 2aR(1-R)\cos(\Delta\varphi). \tag{A.5}$$

If we further assume, that the couplers are ideal 50 : 50 splitter ($R = 0.5$) and there is no loss imbalance between the arms ($a = 1$), we get

$$P_{\mathrm{bar}} = \frac{1}{2} - \frac{1}{2}\cos(\Delta\varphi) \tag{A.6}$$

$$P_{\mathrm{cross}} = \frac{1}{2} + \frac{1}{2}\cos(\Delta\varphi). \tag{A.7}$$

With these simplifications, we can make two observations: For $\Delta\varphi = 0$, all the power is transferred from the first input to the second output port. We call this state the cross-state, and the second output port the cross-port accordingly. For $\Delta\varphi = \pi$, all the power is transferred to the first output port which we call the bar-port. This state is then referred to as the bar-state.

Lastly, we can define the extinction ratio of the cross- and bar-port to be the ratio between the maximum (on-state) and the minimum power transmission (off-state). It is straightforward to see that the minimum power transmission for both ports is 0 in the ideal case, hence the extinction ratio is infinite. If we consider the more realistic case in equations (A.4) and (A.5) we find

$$\mathrm{ER}_{\mathrm{cross}} = \left(\frac{1+a}{1-a}\right)^2, \tag{A.8}$$

$$\mathrm{ER}_{\mathrm{bar}} = \left(\frac{R + a(1-R)}{R - a(1-R)}\right)^2 \tag{A.9}$$

which is discussed further in the main text.

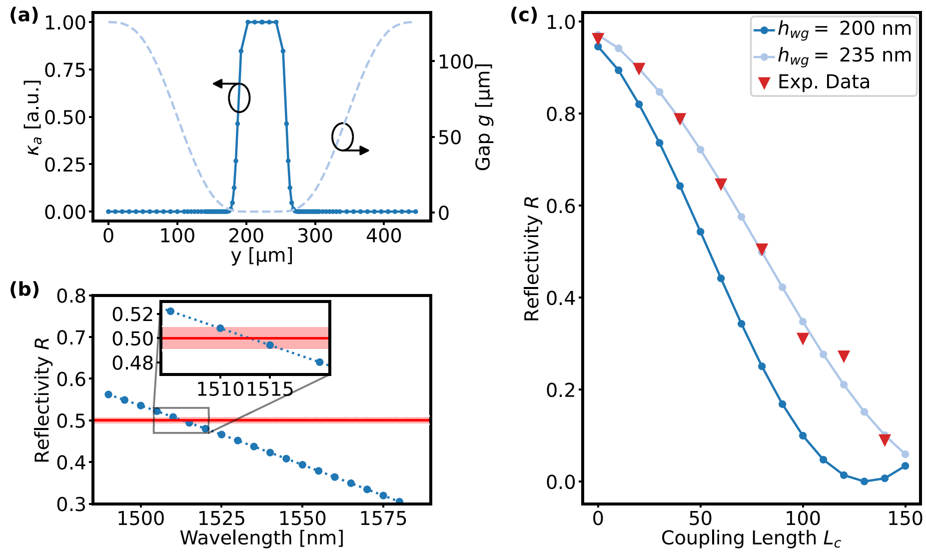

Figure B1. (a) Simulation result of the behavior of the coupling coefficient κ_a along a directional coupler structure (as sketched in figure 2(a)). The secondary y-axis indicates the function $g(y)$ characterizing the gap. (b) Reflectivity of the directional coupler simulated for $h_{\mathrm{wg}} = 235$ nm. The inset is a zoom in to the wavelength region where $R = 0.5$. The red area indicates the $\pm 1\%$ region away from perfect splitting ($R = 0.5$). (c) Comparison of experimental (red triangles) and simulation data for directional coupler reflectivity. Shown are simulation results for waveguide height of 200 nm and 235 nm. The latter match the experimental data better since they take trenching into account.

Appendix B. Directional coupler simulations

In our CMT approach, we consider two waveguides running in parallel. Both of these waveguides support in general a set of eigenmodes. Here we assume we are only interested in the fundamental mode and use $\mathbf{E}_a$ and $\mathbf{E}_b$ to identify them for the two waveguides. We further assume that the fields of the coupled system can be expressed as the sum of the eigenmodes in each waveguide, i.e.

$$\mathbf{E} = A(z)\,\mathbf{E}_a + B(z)\,\mathbf{E}_b. \tag{B.1}$$

The evolution of the amplitudes A and B follow these coupled ordinary differential equations [25]:

$$\frac{\mathrm{d}A}{\mathrm{d}z} = -i\kappa_a B\mathrm{e}^{-\mathrm{i}2\delta z} + i\alpha_a A, \tag{B.2}$$

$$\frac{\mathrm{d}B}{\mathrm{d}z} = -i\kappa_b A\mathrm{e}^{\mathrm{i}2\delta z} + i\alpha_b B, \tag{B.3}$$

where the κ_a and κ_b are the coupling coefficients between the two modes $\mathbf{E}_a$ and $\mathbf{E}_b$, α_a and α_b are the loss factors of the respective mode and the parameter $\delta = \frac{\pi}{\lambda}(n_{\mathrm{eff},a} - n_{\mathrm{eff},b})$.

In figure B1(a) we show an exemplary result for an obtained coupling coefficient κ_a as a function of the position y along the directional coupler. We show the gap $g(y)$ in the same figure. We can see that the coefficient increases as the gap decreases. Furthermore we note, that there is no significant coupling for large gaps, as is expected. Therefore, the simulation time can be reduced by imposing $\kappa_i = 0$ if $g(y) > 10\,\mu$m.

In figure B1(b) the reflectivity R for the device presented in our work as a function of the wavelength is shown. Although the bandwidth is limited, the reflectivity stays within $\pm 1\%$ in a range of 7.0 nm. Further engineering for adiabatic couplers which are wavelength insensitive can increase the bandwidth if required [45].

Our simulations are confirmed with experimental results where we used cascaded directional couplers to extract the coupling ratio which are shown in figure B1(c) (red triangles). Note that these results were obtained on an different 300 nm x-cut LNOI chip without cladding, hence the coupling length is larger than for the directional couplers used in the MZI presented in our work. Simulations with $h_{\mathrm{wg}} = 200$ nm show quite a large offset, whereas simulations with $h_{\mathrm{wg}} = 235$ nm match the experimental data very well. This is due to the trenching inherent to our fabrication process [28]. The trench increases the effective etch depth, which leads to increased mode confinement which in turn reduces the coupling coefficients. Including the trench in our simulations has shown to match better to experimental results, hence the simulation results presented in the main text all consider a waveguide height of $h_{\mathrm{wg}} = 235$ nm.

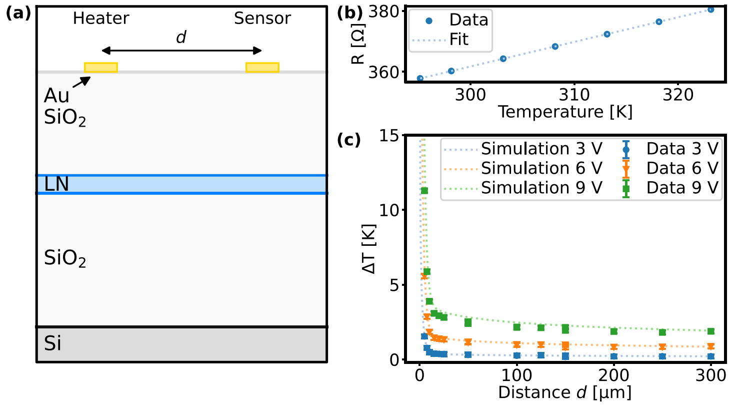

Figure C1. (a) Cross-section of an electrode pair used for measuring the temperature distribution with the heat spreader method. (b) Experimentally measured temperature dependence of the resistance of an electrode. (c) Reconstructed temperature profile for three different applied voltages, along with corresponding simulation values (dotted lines). Simulation and measurement show good agreement.

Appendix C. Characterization of thermal crosstalk

In order to experimentally investigate the thermal crosstalk of the TOPS, we employed the heat spreader method [46]. On an unstructured LNOI chip we fabricated pairs of gold electrodes with the exact dimensions of the heater used on the MZI (i.e. $w_h = 1$ µm, $h_h = 100$ nm and $L_h = 1$ mm) with different center-to-center spacings d between 5 and 300 µm (see figure C1(a)). The fabrication flow is the same that was used for the heater fabrication reported in the main text. During the experiment, we mounted the chip on a temperature controlled mount set to a temperature of $T_0 = 22\,^\circ$C. The electrical connection was done using four needle probes on micromanipulator stages.

First, we characterized a single electrode by sweeping the temperature setpoint of the sample mount and measuring the resistance. It depends linearly on the temperature which is confirmed by the measurement results shown in figure C1(b). Next, for each of the pairs we applied a voltage to one of the electrodes (the heater electrode) and measured the change in resistance ΔR of the other electrode (the sensor electrode). From the first measurement we can then convert the measured ΔR into an estimate for the temperature change ΔT. The results for three different applied voltages are shown in figure C1(c). We compare these values to results of 2D simulations of the heating, which we use instead of the 3D simulations reported in the main text, because the simulation domain becomes too large. We observe good agreement between simulation and measurement.

We can observe a steep decline of the temperature in the first 25 µm which indicates that the heat is well localized around the waveguide of interest. However, there seems to be a small temperature change even at high distances up to 300 µm, observed especially for higher applied voltages. For the spacing between the MZI arms of 127 µm we used, we are outside the region of steep decline, but would expect some small crosstalk. However, for the MZI investigated in this work, the temperature change in the two waveguides is the relevant quantity, which is why crosstalk would only manifest as an increase in power consumption. Since the simulated temperature (see figure 2(d)) in the directly heated waveguide is significantly higher than the temperature in the other waveguide, we believe that this is no significant contribution.

For applications with several interferometers, crosstalk between laterally adjacent MZIs might become an issue. This can be mitigated either by taking it into account in the calibration [47] or by including thermal isolation trenches [37].

Appendix D. Single photon source

In our experiments, we use a BBO crystal for generation of photon pairs. The commerically available crystal is cut for type-II phase matching at a pump wavelength of $\lambda_p = 775$ nm and degenerate signal and idler wavelengths of $\lambda_s = \lambda_i = 1550$ nm. The free-space setup we use is shown in figure D1(a). We use a lens (L1, $f = 75$ mm) to focus the pump beam onto the BBO crystal and a second lens (L2, $f = 50$ mm) to collect the generated photons pairs. A long-pass filter is used to filter the pump and a 12 nm bandpass filter around 1550 nm is used to narrow down the spectrum of the photon pairs. Since a type-II process is used, we can use a polarizing beam splitter (PBS) to deterministically split the signal and idler photons. They are subsequently

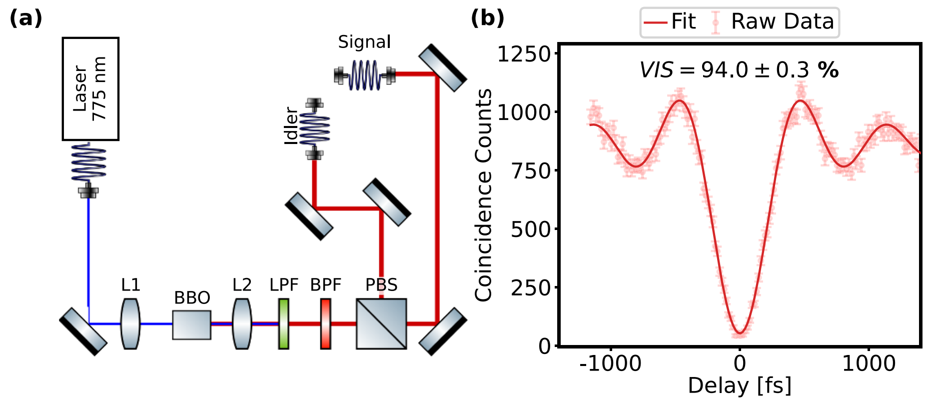

Figure D1. (a) Free space single photon source. The following components are used: (L1): excitation lens; (L2): collection lens; (BBO): BBO crystal; (LPF): Long-pass filter for pump rejection; (BPF): bandpass filter narrowing the photon spectrum; (PBS): Polarizing beamsplitter. (b) Hong-Ou-Mandel interference of the free-space source with visibility of $94.0 \pm 0.3\%$.

coupled to polarization maintaining fiber, where the slow axis of the fiber was aligned to the polarization axis of the respective photon.

To characterize this source, we performed a HOM interference measurement. We use the same fiber-coupled delay lines as for the experiments described in the main text but let the photons interfere on a commercial fiber-coupled beamsplitter. The result of this measurement is shown in figure D1(b), where HOM interference with a visibility of $94.0 \pm 0.3\%$ is observed. We believe that this value is limited by the coupling ratio tolerance which is given as $\pm 1.5\%$ by the manufacturer.

Appendix E. HOM interference measurements

As described in the main text, we performed HOM interference measurements for different voltages applied to the MZI phase shifter. For these measurements we tuned the delay of the two photons as they interfere on the beam splitter and counted the number of coincident detection events on two single photon detectors with a TDC. We consider two events to coincide if they are in a 1 ns window. We assume that these counts are distributed according to a Poissonian distribution, hence the uncertainty of a number of counts N is $\pm\sqrt{N}$. This gives us the errorbars reported in the figures 4(d), (f) and (g), as well as figure E1.

Due to our low countrate and small coupling instabilities, we first apply a Savitzky–Golay filter to the raw data to smoothen the curves which then allows us to fit a curve

$$R(x) = R_{\mathrm{bg}} - A\ \mathrm{sinc}\left(\frac{x-\mu}{\sigma}\right), \tag{E.1}$$

where the background coincidence number R_{bg}, the amplitude A, the mean μ and the parameter σ are fit parameters. The sinc-shape of this curves stems from the fact, that the spectral shape of the photons is given by the 12 nm bandpass filter, which is approximately rectangular. These fits are reported as solid lines in figures 4(d), (f) and (g), as well as figures D1(b) and E1.

Furthermore, we extract the visibilty from the obtained fit parameters as

$$\mathrm{VIS} = 1 - \frac{R_{\mathrm{bg}} - A}{R_{\mathrm{bg}}} = \frac{A}{R_{\mathrm{bg}}}. \tag{E.2}$$

The uncertainty on the visibility is obtained through gaussian error propagation on the uncertainties on the fit parameters A and R_{bg}. However, this method breaks down, as soon as the visibility is on the order of the variation in the filtered coincidence counts, i.e. when there is no visible dip in the measured data anymore. Hence for voltages between 1.5 and 2.75 V, the visibility was estimated using

$$\mathrm{VIS} = 1 - \frac{\min[R(x)]}{\max[R(x)]} \tag{E.3}$$

where the filtered data was used as $R(x)$. The uncertainty in this case is estimated from error propagation of the Poissonian error. The values obtained in this way should be understood as an upper bound on the visibility. The HOM interference dips for all measured voltages are shown in figure E1. The characteristic dip vanishes and reappears as the voltage is increased, which demonstrates the tunability of the integrated device used in the measurement.

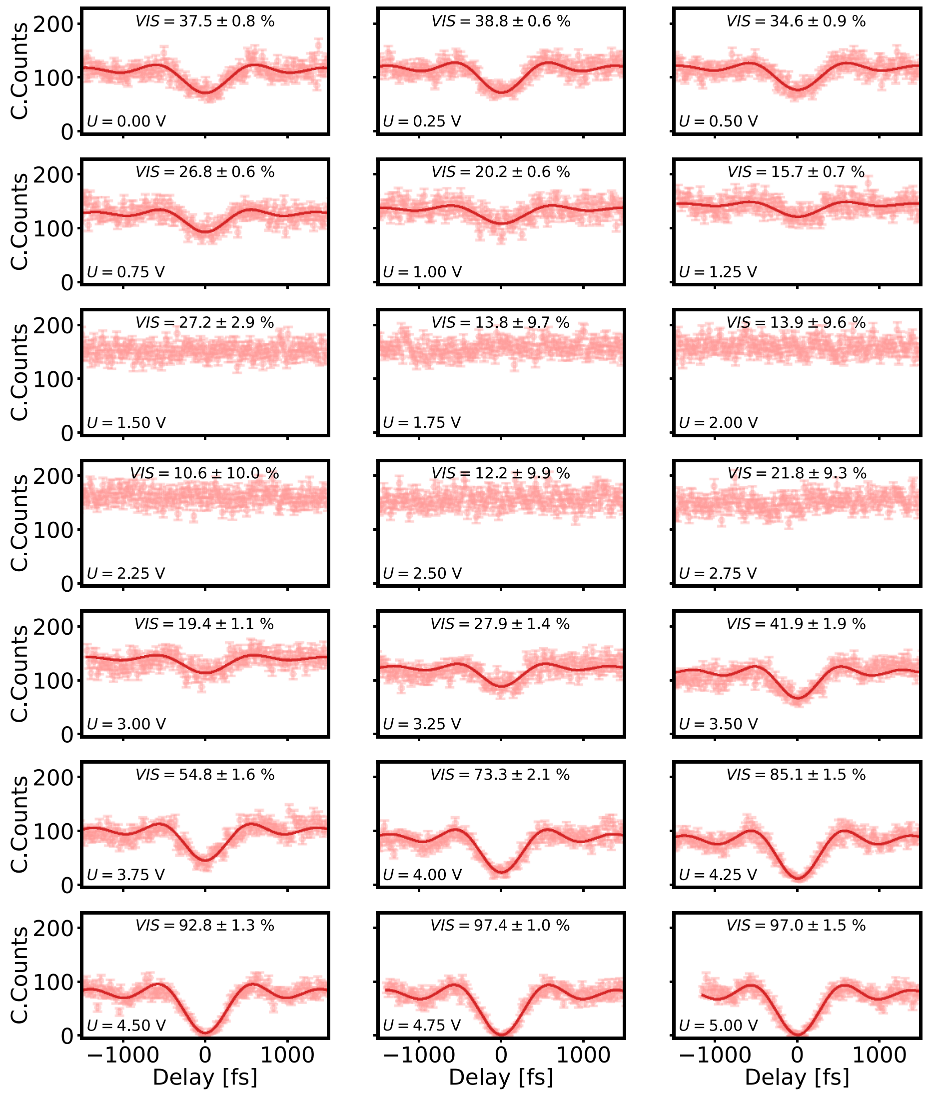

Figure E1. HOM interference measurements for applied voltages between 0 and 5 V. The datapoints correspond to the raw coincidence counts and the solid line, where applicable, is a fit of the expression in equation (E.1). The voltages are indicated in the respective plots and the visibilities correspond to the ones report in figure 3(e) of the main text. Note that estimated visibilites for voltages between 1.5 and 2.75 V should be understood as an upper bound as is described in further detail in the main text and this appendix.

ORCID iDs

Andreas Maeder https://orcid.org/0000-0002-1915-4718
Giovanni Finco https://orcid.org/0000-0002-1218-1924
Fabian Kaufmann https://orcid.org/0000-0002-3164-8833
Alessandra Sabatti https://orcid.org/0009-0003-3233-5147
Jost Kellner https://orcid.org/0000-0003-4037-7489
Robert J Chapman https://orcid.org/0000-0002-0368-8483
Rachel Grange https://orcid.org/0000-0001-7469-9756

References

[1] Aaronson S and Arkhipov A 2011 The computational complexity of linear optics *Proc. 43rd Annual ACM Symp. on Theory of Computing STOC '11' New York, NY, USA* (Association for Computing Machinery) pp 333–42
[2] Knill E, Laflamme R and Milburn G J 2001 *Nature* **409** 46–52
[3] Brod D J, Galv ao E F, Crespi A, Osellame R, Spagnolo N and Sciarrino F 2019 *Adv. Photon.* **1** 034001
[4] Slussarenko S and Pryde G J 2019 *Appl. Phys. Rev.* **6** 041303
[5] Clements W R, Humphreys P C, Metcalf B J, Kolthammer W S and Walmsley I A 2016 *Optica* **3** 1460–5
[6] Wang J *et al* 2018 *Science* **360** 285–91
[7] Carolan J *et al* 2015 *Science* **349** 711–6
[8] Taballione C *et al* 2023 *Quantum* **7** 1071

[9] Boes A, Chang L, Langrock C, Yu M, Zhang M, Lin Q, Lončar M, Fejer M, Bowers J and Mitchell A 2023 *Science* **379** eabj4396
[10] Wolf R, Breunig I, Zappe H and Buse K 2018 *Opt. Express* **26** 19815–20
[11] Desiatov B, Shams-Ansari A, Zhang M, Wang C and Lončar M 2019 *Optica* **6** 380–4
[12] Zhang M, Wang C, Cheng R, Shams-Ansari A and Lončar M 2017 *Optica* **4** 1536–7
[13] Xu M *et al* 2020 *Nat. Commun.* **11** 3911
[14] Pohl D, Messner A, Kaufmann F, Escalé M R, Holzer J, Leuthold J and Grange R 2021 *IEEE Photonics Technol. Lett.* **33** 85–88
[15] Chen Q, Wang M K, Ma X X, Yao H and Chen K X 2022 *IEEE Photon. J.* **14** 1–5
[16] Zhang K, Sun W, Chen Y, Feng H, Zhang Y, Chen Z and Wang C 2023 *Commun. Phys.* **6** 17
[17] Zhao J, Ma C, Rüsing M and Mookherjea S 2020 *Phys. Rev. Lett.* **124** 163603
[18] Sund P I *et al* 2023 *Sci. Adv.* **9** eadg7268
[19] Holzgrafe J C 2022 Cavity electro-optics in thin-film lithium niobate *PhD Thesis* Harvard University United States – Massachusetts
[20] Salvestrini J P, Guilbert L, Fontana M , Abarkan M and Gille S 2011 *J. Lightwave Technol.* **29** 1522–34
[21] Maeder A, Kaufmann F, Pohl D, Kellner J and Grange R 2022 *Opt. Lett.* **47** 4375–8
[22] Chen G, Lin H-L, Ng J D and Danner A J 2021 *IEEE Photonics Technol. Lett.* **33** 664–7
[23] Lund A P, Laing A, Rahimi-Keshari S, Rudolph T, O'Brien J L and Ralph T C 2014 *Phys. Rev. Lett.* **113** 100502
[24] Hamilton C S, Kruse R, Sansoni L, Barkhofen S, Silberhorn C and Jex I 2017 *Phys. Rev. Lett.* **119** 170501
[25] Okamoto K 2006 *Chapter 4-Coupled Mode Theory Fundamentals of Optical Waveguides* 2nd edn ed K Okamoto (Academic) pp 159–207
[26] Liu S, Feng J, Tian Y, Zhao H, Jin L, Ouyang B, Zhu J and Guo J 2022 *Front. Optoelectron.* **15** 9
[27] Moretti L, Iodice M, Della Corte F G and Rendina I 2005 *J. Appl. Phys.* **98** 036101
[28] Kaufmann F, Finco G, Maeder A and Grange R 2023 *J. Nanophoton.* **12** 1601–11
[29] Okamoto M, Mendez-Astudillo M and Kita T 2020 *Jpn. J. Appl. Phys.* **59** SOOA03
[30] Geis M, Spector S, Williamson R and Lyszczarz T 2004 *IEEE Photonics Technol. Lett.* **16** 2514–6
[31] Babel S *et al* 2023 *Opt. Express* **31** 23140–8
[32] Flamini F *et al* 2015 *Light: Sci. Appl.* **4** e354
[33] Matthews J C F, Politi A, Stefanov A and O'Brien J L 2009 *Nat. Photon.* **3** 346–50
[34] Taballione C *et al* 2021 *Mater. Quantum Technol.* **1** 035002
[35] Wang M, Li J, Yao H, Li X, Wu J, Chiang K S and Chen K 2022 *Opt. Express* **30** 39706–15
[36] Song L, Liu W, Guo Z, Li H, Xie Y, Yu Z, Li H, Shi Y and Dai D 2023 *Laser Photon. Rev.* **17** 2300025
[37] Ying P, Tan H, Zhang J, He M, Xu M, Liu X, Ge R, Zhu Y, Liu C and Cai X 2021 *Opt. Lett.* **46** 1478–81
[38] Papon C, Zhou X, Thyrrestrup H, Liu Z, Stobbe S, Schott R, Wieck A D, Ludwig A, Lodahl P and Midolo L 2019 *Optica* **6** 524–30
[39] Saha U, Siverns J D, Hannegan J, Prabhu M, Quraishi Q, Englund D and Waks E 2023 *Phys. Rev. Appl.* **19** 034001
[40] Wilkes C M, Qiang X, Wang J, Santagati R, Paesani S, Zhou X, Miller D a B, Marshall G D, Thompson M G and O'Brien J L 2016 *Opt. Lett.* **41** 5318–21
[41] Jin M, Chen J Y, Sua Y M and Huang Y P 2019 *Opt. Lett.* **44** 1265–8
[42] Gao Y, Lei F, Girardi M, Ye Z, Laer R V, Torres-Company V and Schröder J 2023 *Opt. Lett.* **48** 3949–52
[43] Lomonte E, Wolff M A, Beutel F, Ferrari S, Schuck C, Pernice W H P and Lenzini F 2021 *Nat. Commun.* **12** 6847
[44] Prencipe A *et al* 2023 *Nano Lett.* **21** 9748–52
[45] Mao D *et al* 2019 *J. Lightwave Technol.* **37** 6147–55
[46] Dames C 2013 *Annu. Rev. Heat Transf.* **16** 7–49
[47] Pentangelo C, Giano N D, Piacentini S, Arpe R, Ceccarelli F, Crespi A and Osellame R 2024 *Nanophotonics* **13** 2259–70